PAPER • **OPEN ACCESS**

UV photodetectors based on W-doped ZnO thin films

To cite this article: R Jalal *et al* 2024 *Nanotechnology* **35** 265705

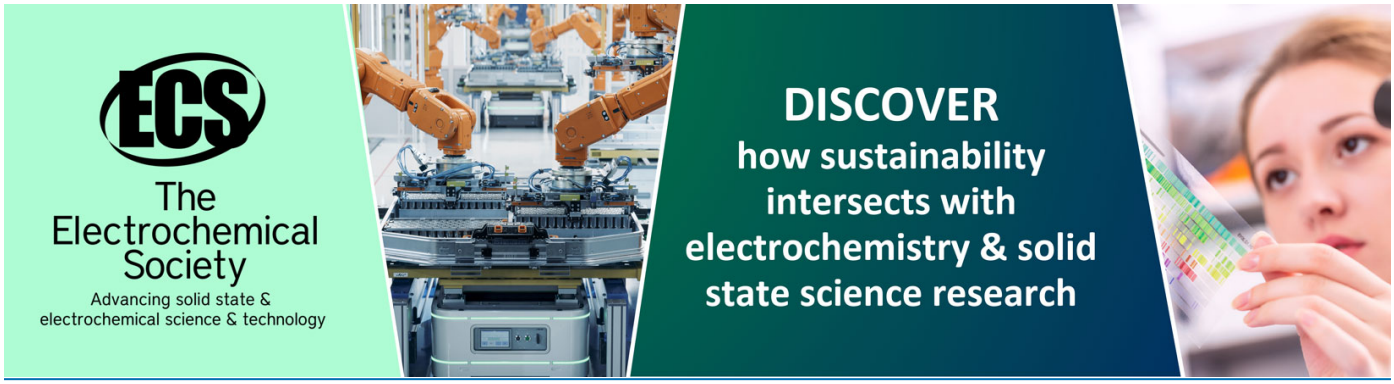
View the article online for updates and enhancements.

You may also like

- W-Doping of Dense NMC811 Hydroxide through Wet-Impregnation and Its Impact on Crystal Structure, Phase Transition Related Gas Evolution and Electrochemical Performance at Elevated Upper Cut-Off Voltage
Mert Dalkilic, Alexander Schmidt, Thomas D. Schladt et al.

- Detailed pathway for a fast low-temperature synthesis of strongly thermochromic W-doped VO_2 films with a low transition temperature
Jaroslav Vlek, Michal Kaufman, Andrea Dagmar Pajdarová et al.

- Influence of defects and doping on phonon transport properties of monolayer $MoSe_2$
Zhequan Yan, Mina Yoon and Satish Kumar



This content was downloaded from IP address 95.183.211.218 on 28/04/2024 at 22:04

OPEN ACCESS
IOP Publishing
Nanotechnology
Nanotechnology **35** (2024) 265705 (10pp)
https://doi.org/10.1088/1361-6528/ad373b

UV photodetectors based on W-doped ZnO thin films

R Jalal[1], K Ozel[2], A Atilgan[1] and A Yildiz[1]

[1] Department of Energy Systems Engineering, Faculty of Engineering and Natural Sciences, Ankara Yıldırım Beyazıt University, Ankara, 06010, Turkey
[2] Department of Electrical and Energy, GAMA Vocational School, Ankara University, Ankara, 06120, Turkey

E-mail: kenanozel89@gmail.com

Received 31 October 2023, revised 26 January 2024
Accepted for publication 24 March 2024
Published 9 April 2024

Abstract

W-doped ZnO thin films deposited on Si substrates with (100) orientation by sol–gel spin coating method at temperature 500 °C. W/Zn atomic ratio varies from 0% to 4%. Then, the UV detection performance analysis of *p–n* heterojunction UV photodetectors based on W-doped ZnO/Si is analyzed. The current–voltage curves of W-doped ZnO/Si are investigated in dark and exhibit diode-like rectifying behavior. Among doped ZnO/Si, sample with atomic ratio of W/Zn = 2% is the best candidate to study photodetector characteristics in UV range. The resulting device exhibits a rectification ratio *RR* of 5587 at ±5 V, a higher responsivity of 3.84 A W^{-1} and a photosensitivity value of 34 at 365 nm under 0.5 mW cm^{-2}. The experimental findings reveal that the UV detection performance of the heterojunction-based photodetectors strongly dependent on the properties of metal oxide layer. The main goal of this work is to investigate the effect of W doping on the performance of ZnO/Si based photodetectors. Based on our results, it is observed that 2 at% of W dopant is the optimum amount of doping for high performance photodetector of ZnO:W/Si heterojunction thanks to the suppressed recombination ratio and enhanced carrier separation properties in the depletion zone.

Keywords: tungsten doping, ZnO thin films, heterojunction, photodetectors

1. Introduction

In the realm of optoelectronics, photodetectors play a pivotal role in converting light signals into electrical signals. They are widely used in various applications such as imaging, communication systems, sensing technologies, and missile warning systems [1–3]. The working principle of a photodetector is based on the phenomenon of photoconductivity. When light strikes the surface of a photosensitive material, it excites the electrons within the material, causing them to transition from the valence band to the conduction band. This process generates electron–hole pairs, resulting in an increase in electrical conductivity within the material [4].

Up to now, photodetectors have been designed in many different structures such as metal–semiconductor–metal (MSM), metal–insulator–metal (MIS), *p–n* homojunction or heterojunction [5–7]. In recent years, metal oxide-based heterojunctions have gained significant importance in the fabrication of advanced photonic and electronic devices. Particularly, the integration of metal oxide on rigid or flexible substrates has been a key focus of research and development [8, 9]. In this regard, zinc oxide (ZnO) has emerged as a highly preferred material for various applications such as photovoltaics, photodetection, and photocatalysis, thanks to its favorable properties including a wide bandgap, long-term chemical stability, easy availability, and non-toxicity [10]. Additionally, the optical and electrical properties of ZnO can be optimized by doping with some elements including manganese (Mg) [11], cobalt (Co) [12], aluminum (Al) [13], gallium (Ga) [14], indium (In) [15], and tungsten (W) [16]. Among them, tungsten trioxide attracts attention thanks to its favorable optoelectronic features [17]. Besides, it has also

Original content from this work may be used under the terms of the Creative Commons Attribution 4.0 licence. Any further distribution of this work must maintain attribution to the author(s) and the title of the work, journal citation and DOI.

© 2024 The Author(s). Published by IOP Publishing Ltd

been reported that tungsten-doping leads to improved photocatalytic activity, high structural stability and enhanced optoelectrical property [18–20].

In this study, we have achieved a successful deposition of pure ZnO and various concentrations (0.5 at%, 1 at%, 2 at%, and 4 at%) of tungsten-doped ZnO onto a *p*-silicon substrate utilizing the sol–gel spin coating method. Through characterization of the fabricated sample, we evaluated its performance in UV detection and conducted a quantitative comparison with *p–n* heterojunction analogues, considering multiple performance parameters. Notably, we discovered that the device designed with a 2 at% of W doping exhibited exceptional performance, demonstrating a remarkable photoresponsivity of 3.84 A W^{-1} at 365 nm together with high detectivity of 3.30 $\times$ 10^{12} Jones, large external quantum efficiency of 1305% and high linear dynamic range of 30.63 dB. This breakthrough sets the stage for cost-effective manufacturing of high-performance devices.

2. Experimental

The undoped and 0.5 at%, 1 at%, 2 at%, and 4 at% of W-doped ZnO (WZO) films were spin-coated onto square glass substrates (25 $\times$ 25 mm^2) (ISOLAB glass) of superior quality. The solution for spin coating was prepared by dissolving zinc acetate dihydrate, ZAD ($ZnC_4H_6O_4.2H_2O$; EMSUR), and tungsten (VI) chloride, WCl_6 (ALDRICH, 99.9% trace metals base) in ethanol (C_2H_6O; EMSUR), followed by the addition of a monoethanolamide, MEA (C_2H_7NO; EMSUR, 99.5%) stabilizer. The concentration of ZAD in the ethanol solvent was 0.6 M, and the MEA:ZAD molar ratio was maintained at 1:1. The concentration of W dopant ([nW/[nW+nZn]) was calculated to be 0.5%, 1%, 2%, and 4 at%, respectively. Using a magnetic stirrer, the resultant mixtures were stirred for 2 h at 60 °C to obtain a clear, transparent, and homogenous solution. Before being utilized as a coating solution, the solution was aged for 48 h at room temperature. In brief, it is noteworthy to mention that some factors including concentration, aging time, deposition technique, annealing temperature, etc affect the properties of the thin films [21, 22]. In particular, it has been reported that solution aging time changes the optical, structural and electrical properties of the thin film [23]. The results of investigation on the effect of aging on ZnO thin films show that 48 h is the optimum aging time for achieving high grain size and low defect density [24].

Prior to deposition, Al conductive paste was applied to the bottom of pre-cleaned *p*-Si substrates by using screen-printing method. Five cycles of coating were applied in spin coating method to deposit undoped and W-doped ZnO (WZO) films on pre-cleaned *p*-Si substrates. The deposition of WZO films was carried out at a spinning speed of 2000 rpm for a duration of 30 s. After each spin coating process, the deposited films were dried at 500 °C for 5 min. The coating-drying process were repeated five times, and the obtained films were annealed at 500 °C for 1 h to get the polycrystalline thin-films. Subsequently, the grid-shaped front contacts of the samples were achieved by using Ag conductive paste.

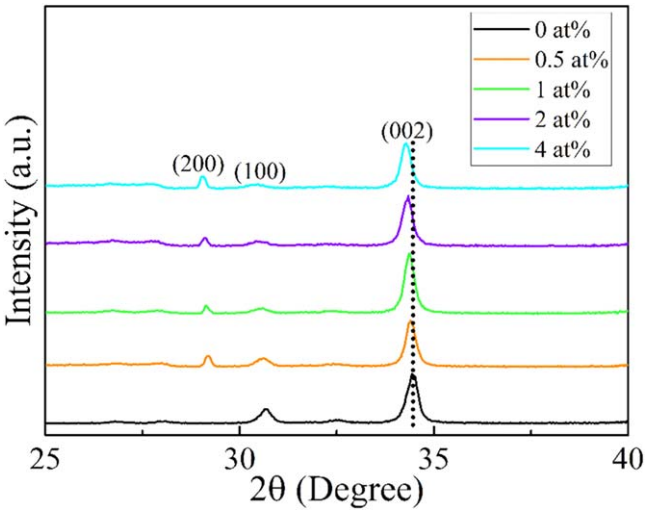


Figure 1. XRD pattern of the undoped and W-doped ZnO thin films.

X-ray diffraction (Rigaku Miniflex 600) measurements were accomplished to evaluate the structural properties of ZnO and W doped-ZnO films. Scanning electron microscopy (SEM) (Hitachi SU5000) was utilized to characterize the surface morphology of the films. Also, the thickness of W-ZnO layer was determined from cross-sectional SEM measurement. UV–vis spectrophotometer (Shimadzu 1700) was used to estimate the optical profiles of the films. The current–voltage (*I–V*) characteristics were determined using semiconductor measurement unit (Keithley 2400) in the dark and under UV light of 365 nm (0.5 mW cm^{-2}). The capacitance–voltage (*C–V*) profiles of the devices were measured at a frequency of 100 kHz in the dark.

3. Results and discussions

Figure 1 displays the XRD patterns of undoped and W-doped ZnO films with various doping percentage. The crystal peaks of (200), (100) and (002) are observed for all the samples. Peaks in the data are consistent with the ZnO structure described by JCPDS 01-084-3901.

A strong peak at about $2\theta = 34.5°$, corresponding to the (002) peak indicates that the samples with hexagonal structures having a preferred orientation perpendicular to the substrate. The position of (002) peak slightly shifts to the left with increasing W percentage. Doping of W leads no additional peaks belonging secondary phase of W, unveiling that that Zn ion sites are replaced by W ions in the lattice. Crystallite size of the samples (*D*) calculated by Debye-Scherer formula [25] is given in table 1. As seen, the value of *D* slightly increases to some extent after W incorporation in ZnO lattice, suggesting an improvement in crystallinity, and then decreases upon further increasing the W content. The size of the crystallites was found to decrease as the concentration of W increased further. It indicates that the higher concentration of W can obstruct the movement of the grain boundary, causing to the formation of smaller particles by limiting the grain growth [26, 27]. Dilawar *et al* reported similar results for La and Sm doped ZnO thin

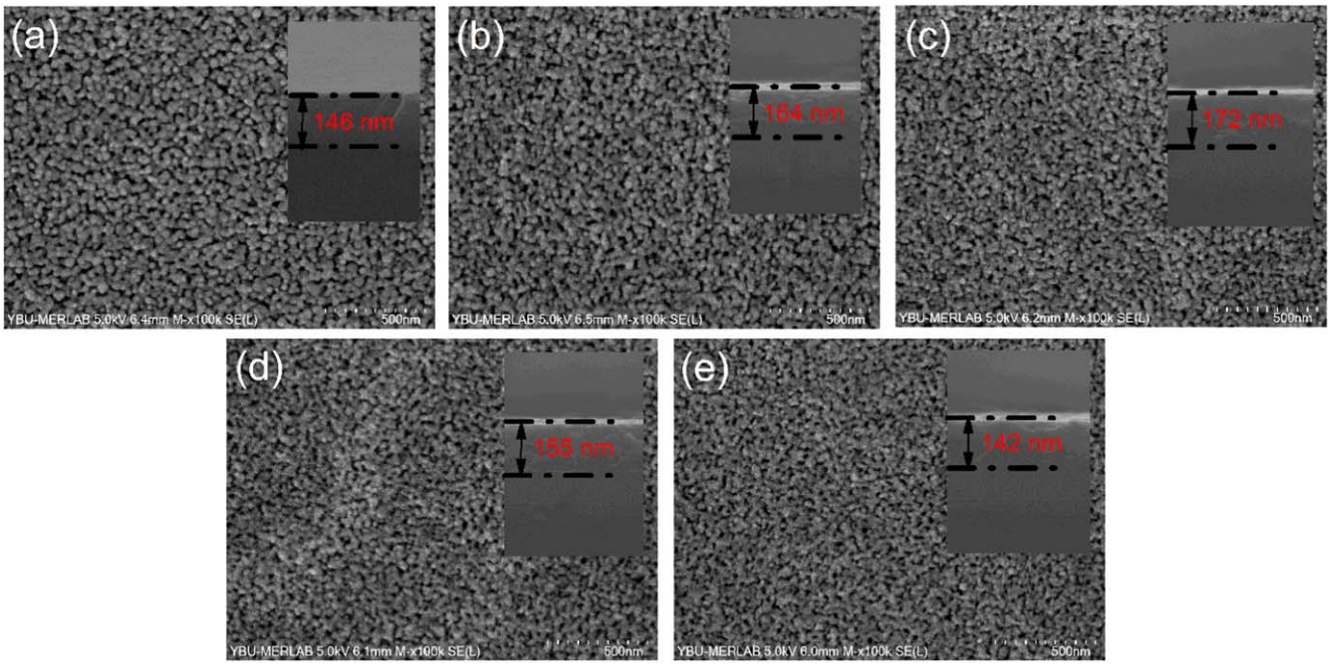


Figure 2. SEM images of the undoped and W-doped ZnO thin films. The inset figures demonstrate the side-view SEM images of the films. The thickness values are estimated from cross-sectional SEM image as 146, 164, 172, 155 and 142 nm for (a) undoped, and (b) 0.5%, (c) 1%, (d) 2%, and (e) 4 at% of W doped ZnO, respectively.

Table 1. Various parameters estimated from XRD, UV–vis, SEM and four-point probe.

Sample (W at%)	Thickness (nm)	D (nm)	T_{av} (%)	E_g (eV)	R_{sh} (MΩ/sq)	ρ (Ω.cm)	FOM ($\times 10^{-7}$ Ω^{-1})
0	146	27.5	76.5	3.132	98.34	14.357	0.379 604
0.5	164	31.1	79.9	3.163	80.66	13.228	0.552 497
1	172	31.3	82.3	3.184	63.87	10.985	0.803 741
2	155	30.3	83.6	3.191	47.55	7.370	1.174 057
4	142	29.6	82.8	3.198	54.82	7.784	0.966 478

films [28]. In addition, lattice strain has an impact on the decreasing in crystallinity [29].

Surface morphology of the undoped and W-doped ZnO thin films formed at various W percentages is shown in figure 2. According to SEM images, the substrate is completely coated in numerous compact grains that are uniformly distributed. Porous regions are also seen in the samples. From the results, one can comprehend that the change in doping concentration plays little role in the differentiation of the surface morphologies of the films. The inset of figure 2 indicates the cross-sectional SEM image of the undoped and W-doped ZnO thin films. To carefully investigate the effect of W doping on the properties of ZnO films, all the WZO films were deposited under the same experimental conditions including the factors of solution concentration, aging time, spinning speed, annealing temperature, etc. Hence, the thickness value of the films is measured to be in range of ∼140–170 nm.

To determine the impact of the W doping on transmittance (T) and energy band gap (E_g) of ZnO, ultraviolet-visible (UV–vis) absorption of the samples are measured, the results of which are presented in figure 3. Average transmittance (T_{av}) value taken in visible region gradually increases with W dopant and reaches a maximum value of 83.6% at 2 at% of W doping (table 1). Then, it drops with further doping of 4 at% of W. Herein, ZnO layer will be used as an n-type layer to form *p–n* heterojunction. In this respect, therefore, 2 at% of W doping seems to be the best candidate being used in the device. The inset of figure 3 shows Tauc's plot which is employed to estimate E_g values [30]. Accordingly, the incorporation of W dopant in ZnO results in a blue shift in the absorption edge (table 1).

To determine the resistivity of the films, the sheet resistance (R_{sh}) values are calculated using the following equation [31].

$$R_{sh} = \frac{\pi}{\ln(2)}\left(\frac{V}{I}\right) = 4.532\left(\frac{V}{I}\right) \quad (1)$$

where, 4.532 is the correction factor, V and I refer to the measured voltage and current passing through the film, respectively. Once the values of R_{sh} and thickness (t) are known, the resistivity of the films can be obtained utilizing the equation of $\rho = R_{sh}t$ [31]. To judge the quality of thin films in terms of their both optical and electrical characteristics, the figure of merit (FOM) values of the films are determined using the equation of $FOM = -1/[R_{sh}\ln(T)]$ [32].

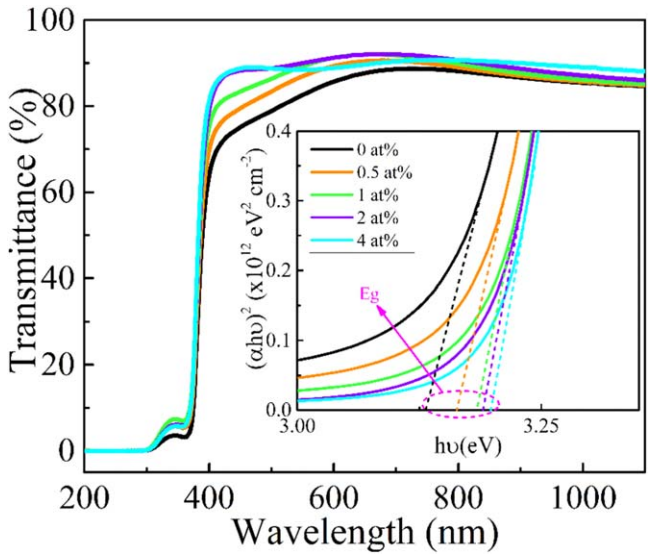


Figure 3. Transmittance characteristics of W-ZnO layers. The inset demonstrates Tauc's plot.

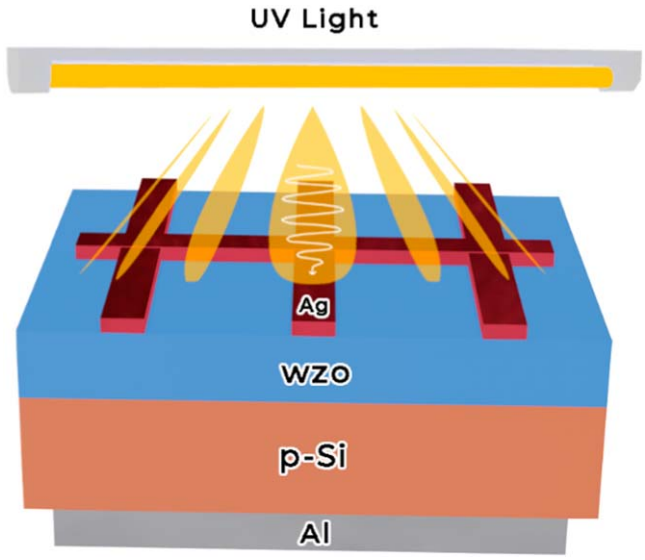


Figure 5. Schematic representation of W-ZnO/*p*-Si based device.

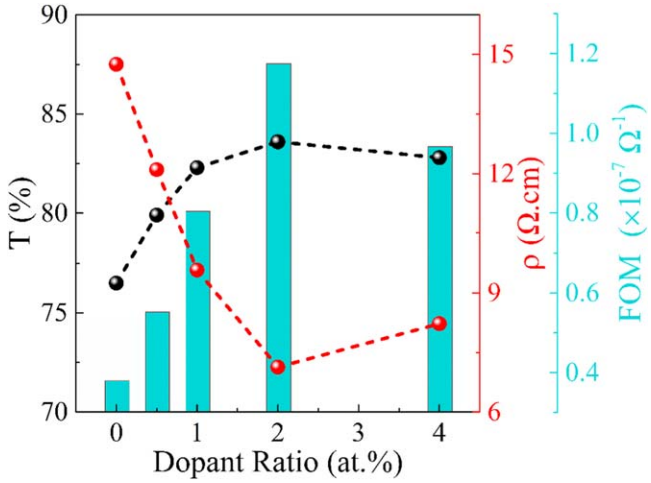


Figure 4. The variation of T_{av}, ρ and *FOM* as a function of dopant ratio for the WZO films.

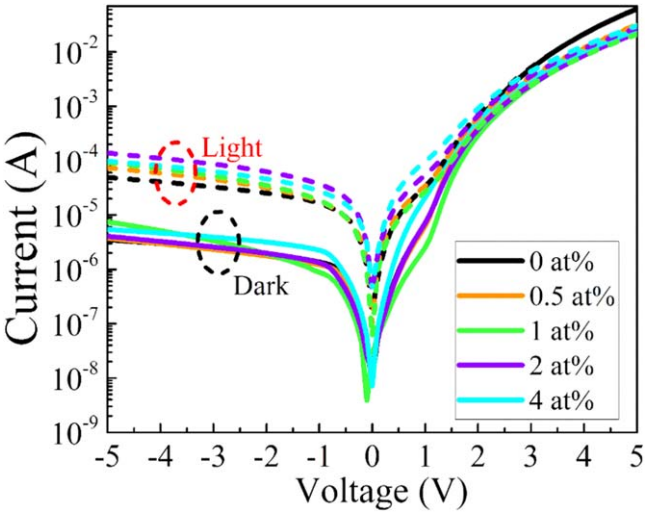


Figure 6. Current–voltage (*I–V*) characteristics for the fabricated devices.

The *FOM* values of the samples are found to be as 0.0379, 0.0552, 0.0803, 0.1174, and 0.0966 $\mu\Omega^{-1}$ for undoped and 0.5 at%, 1 at%, 2 at%, and 4 at% of W-doped ZnO (WZO) films. A higher *FOM* value indicates that the sample has superior performance in terms of optoelectronic properties. It can be observed that the 2 at% of W-doped ZnO (WZO) film reaches the highest *FOM* value of $1.174 \times 10^{-7}\,\Omega^{-1}$ thanks to its high transparency and low resistivity. The calculated values of R_{sh}, ρ and *FOM* are summarized in table 1. Note that the obtained values of R_{sh}, ρ and *FOM* are consistent with the reported ones [16, 33]. Figure 4 shows the variation of T_{av}, ρ and *FOM* as a function of dopant ratio for the WZO films. It can be seen that the resistivity of the films decreases with increasing dopant concentration, and gets lowest value for 2 at% of W-doped ZnO film. This decrease in resistivity can be explained by the increased number of free electrons of donors W^{6+} ions occupying the locations of Zn^{2+} cations [34]. On the other hand, the resistivity of the films exhibits an increasing trend above 2 at% doping of W, which might be the result of dopant atoms segregating at the grain boundaries and causing disturbances in the lattice [35].

Figure 5 depicts the schematic of the studied photodetectors. All electrical measurements are carried out under ambient conditions at room temperature. Prior to measuring *p–n* photodetector performance, the contacts to W-ZnO and Si on Ag/WZO and Al/Si junctions are separately tested using linear *I–V* characteristics [36, 37]. As we verified elsewhere, they exhibit Ohmic behavior proving that Schottky behavior rises from a *p–n* junction occurring between ZnO and Si.

Figure 6 shows the *I–V* characteristics of the UV detector recorded in dark and under 365 nm light illumination at different bias voltages range from −5 to +5 V. The devices respond to a wavelength of 365 nm of light, displaying

Table 2. Photodetector parameters of undoped and W-doped ZnO thin films-based devices.

Sample (% at W)	*RR*	*PR* (A/W)	*PS*	D^* x10^{12} (Jones)	*EQE* (%)	*LDR* (dB)	*NEP* $\times 10^{-13}$ (W/Hz$^{1/2}$)
0	17733	1.30	14.03	1.23	519	22.94	8.13
0.5	8224	1.99	19.56	1.82	675	25.83	5.51
1	3658	2.43	12.41	1.57	825	21.87	6.36
2	5587	3.84	34.01	3.30	1305	30.63	2.97
4	4664	2.65	18.09	2.01	901	25.15	4.97

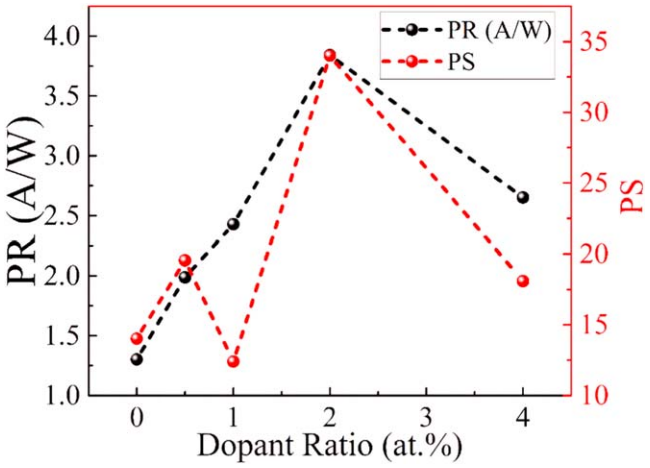


Figure 7. Photoresponsivity (*PR*) and photosensitivity (*PS*) versus dopant ratio plots of the devices.

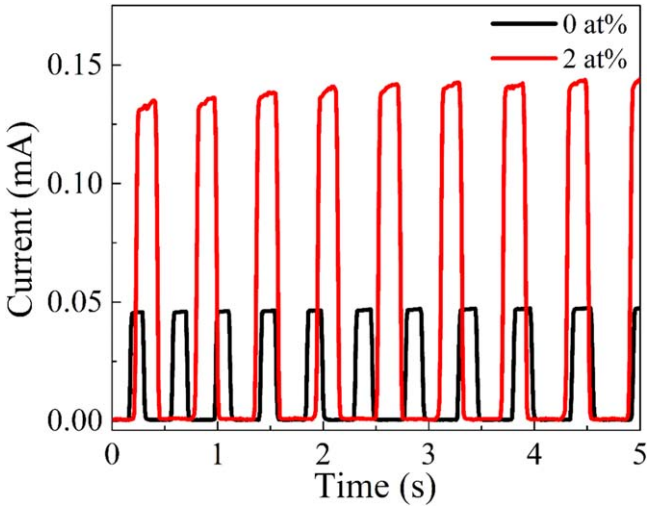


Figure 8. The time-dependent photoresponse characteristics of the devices consist of undoped and 2 at% of W doped ZnO.

increased current as compared to that in the dark. An excellent rectifying behavior and low dark current of the devices, which originate from the high-quality junction between *n*-ZnO and *p*-Si layers, are readily apparent when their rectification performance is assessed. Even though the rectification ratio ($RR = I_{\text{forward}}/I_{\text{reverse}}$) of W-doped ZnO layer-based devices is lower than that of undoped ZnO layer-based device at the bias of ±5 V (table 2), the observed *RR* values are superior to those reported for similar structures [38, 39]. Accordingly, the photocurrent induced by the light at a wavelength of 365 nm can be ascribed to the electron–hole pairs generated by the incident photons with wavelength smaller than the wavelength (380 nm) corresponding to bandgap. It is obvious that the devices exhibit an exceptional photoresponse when exposed to 365 nm light illumination. The photoresponsivity (*PR*) is defined as [40];

$$PR = \frac{I_{\text{light}}}{P_\lambda A} \tag{2}$$

where I_{light}, P_λ and A stand for the photocurrent, the intensity of illuminating light, and the effective area (1 cm^2), respectively. The *PR* represents the photocurrent produced per unit of the intensity of illuminating light. The *PR* values calculated at a reverse bias of 5 V are given in table 2, which is improved by incorporating of W dopant. Another key parameter is the photosensitivity (*PS*) which is expressed as [41];

$$PS = \frac{I_{\text{light}} - I_{\text{dark}}}{I_{\text{dark}}} \tag{3}$$

where I_{dark} is the current in the dark. As seen from table 2, the *PS* can be improved by incorporating of W dopant as well. This proposes to boost the performance of ZnO/Si heterojunction structure, W dopant should be employed in ZnO lattice. In figure 7, these photodetector metrics for the devices are compared under different W-dopant percentages. This comparative plot illustrates that 2 at% of W-doped ZnO has clear advantages compared to others, providing 2.95-fold higher photoresponsivity and 2.42-fold greater photosensitivity.

Other vital photodetector metrics are the specific detectivity ($D*$), the external quantum efficiency (*EQE*), linear dynamic range (*LDR*) and noise equivalent power (*NEP*). The $D*$, *EQE*, *LDR* and *NEP* evaluate the sensitivity to weak optical signals, the photon utilization rate, signal-to-noise ratio, and the input illumination power to generate a signal-to-noise ratio of 1 at bandwidth of 1 Hz, respectively. They can be estimated by [40, 42];

$$D^* = \frac{PRA^{1/2}}{(2qI_{\text{dark}})^{1/2}} \tag{4}$$

$$EQE = \frac{hc}{q\lambda} PR \times 10^2\% \tag{5}$$

$$LDR = 20\log\left(\frac{I_{\text{light}}}{I_{\text{dark}}}\right) \tag{6}$$

$$NEP = \frac{A^{1/2}}{D^*} \tag{7}$$

where q, h, c and λ denote unit charge, Planck's constant, the speed of light and the excitation wavelength, respectively.

Table 3. Comparison of the photodetector parameters of current work with those reported for doped ZnO photodetectors.

Sample	τ_r(s)	*PR* (A/W)	*PS*	*D*∗ (Jones)	*EQE* (%)	References
ZnO:Ni	0.5	7.52×10^{-6}	416	7.92×10^{8}	—	[44]
ZnO:Co	1.4	0.93	—	9.32×10^{10}	218	[45]
ZnO:Sn	3	1.56	1.2×10^{5}	1.70×10^{10}	—	[46]
ZnO:Ga	1	0.38	—	1.24×10^{10}	125	[47]
ZnO:Nd	0.3	0.73	—	1.18×10^{11}	236	[48]
ZnO:Al	30	3.65	—	1.30×10^{12}	—	[49]
ZnO:Cd	5	2.96×10^{-5}	920	2.4×10^{9}	—	[50]
ZnO:Fe	46	0.75	471			[51]
ZnO:W	0.025	3.84	34.01	3.30×10^{12}	1305	This work

Table 4. The parameters extracted from figure 8.

Sample (at % of W)	$N_d \times 10^{16}$ (cm^{-3})	d_n (nm)	d_p (nm)	W (nm)	V_{bi} (V)
0	1.36	119	381	500	0.68
0.5	1.91	91	391	482	0.69
1	2.26	73	440	513	0.69
2	4.97	35	475	510	0.71
4	10.3	18	484	502	0.73

With amount of W-dopant rises, the recombination ratio of electron–hole pairs is initially suppressed until 2 at% of W dopant, then the recombination ratio is boosted with further increase in amount of W-dopant to 4 at% because of the increased concentration of charge carriers. Therefore, both *D*∗ and *EQE* are initially improved until 2 at% of W dopant then reduced. *D*∗ and *EQE* reach maximum values of 3.3×10^{12} Jones and 1305% at 2 at% of W dopant, implying a good ability for weak signal detection and a significant improvement in proportion of photoexcited electron–hole pairs. Notably, the device including 2 at% of W dopant exhibits a remarkable *LDR* and *NEP* value with the trend observed in other figures of merit. The *LDR* is estimated to be ∼31 dB at 2 at% of W dopant. This value is much larger than that of the device including undoped ZnO, demonstrating a significant photocurrent to dark current ratio and a strong signal-to-noise ratio. The *NEP* of 2.97×10^{-13} W/$Hz^{1/2}$ is achieved at 2 at% of W dopant. The ultralow *NEP* stands for the low noise ratio, which increases the sensitivity of the detector to optical signals. The above results reveal that 2 at% of W dopant is the more suitable amount of doping for high performance photodetector of ZnO:W/Si heterojunction.

The time-resolved photoresponse plots of the photodetectors consisting of undoped and 2 at% of W doped ZnO at a reverse bias of 5 V are shown in figure 8. The rise time (τ_r) /decay time (τ_d) are assumed to be 19, 17 ms, respectively for undoped one, and 25, 20 ms, respectively for 2 at% of W doped ZnO one. Generally, there is a trade-off between photoresponsivity and response time [43]. Therefore, such a response speed is meaningful concerning high photoresponsivity of W-doped ZnO with respect to undoped one.

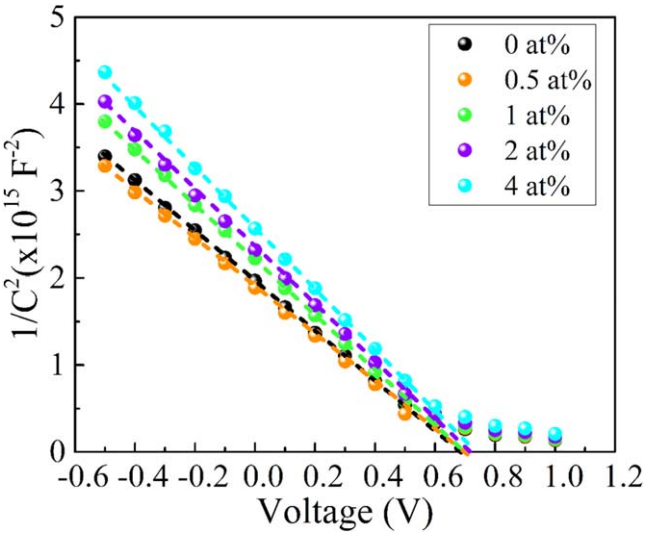


Figure 9. $1/C^2$–V curves of the devices.

The performance comparison of the photodetector parameters of current work with those reported for doped ZnO photodetectors is given in table 3. It is worth noting that the τ_r, *PR*, *D*∗, and *EQE* in our device are better than other reported photodetectors. The rapid separation and collection of photogenerated carriers in our device is primarily responsible for the impressive performance we achieve in the present investigation. In addition to this, the superior carrier transport property of W-doped ZnO makes it advantageous for the rapid drift of charge carriers, resulting in a short response time.

To get insight into the underlying physics of this high performance of the device having 2% W dopant rate, the capacitance (C)–voltage (V) measurements are carried out for the devices. As shown in figure 9, the slope and x-intercept of $1/C^2$ versus voltage characteristics are used to estimate the values of donor concentration (N_d) and built-in potential (V_{bi}) [52]. The heterojunction theory can be used to express the depletion layer capacitance [37].

$$C^2 = \frac{qN_aN_d\varepsilon_1\varepsilon_2}{2(N_d\varepsilon_1 + N_a\varepsilon_2)}\frac{1}{V_{bi} - V} \tag{8}$$

where N_d, V, ε_1 and ε_2 refer to donor concentration and

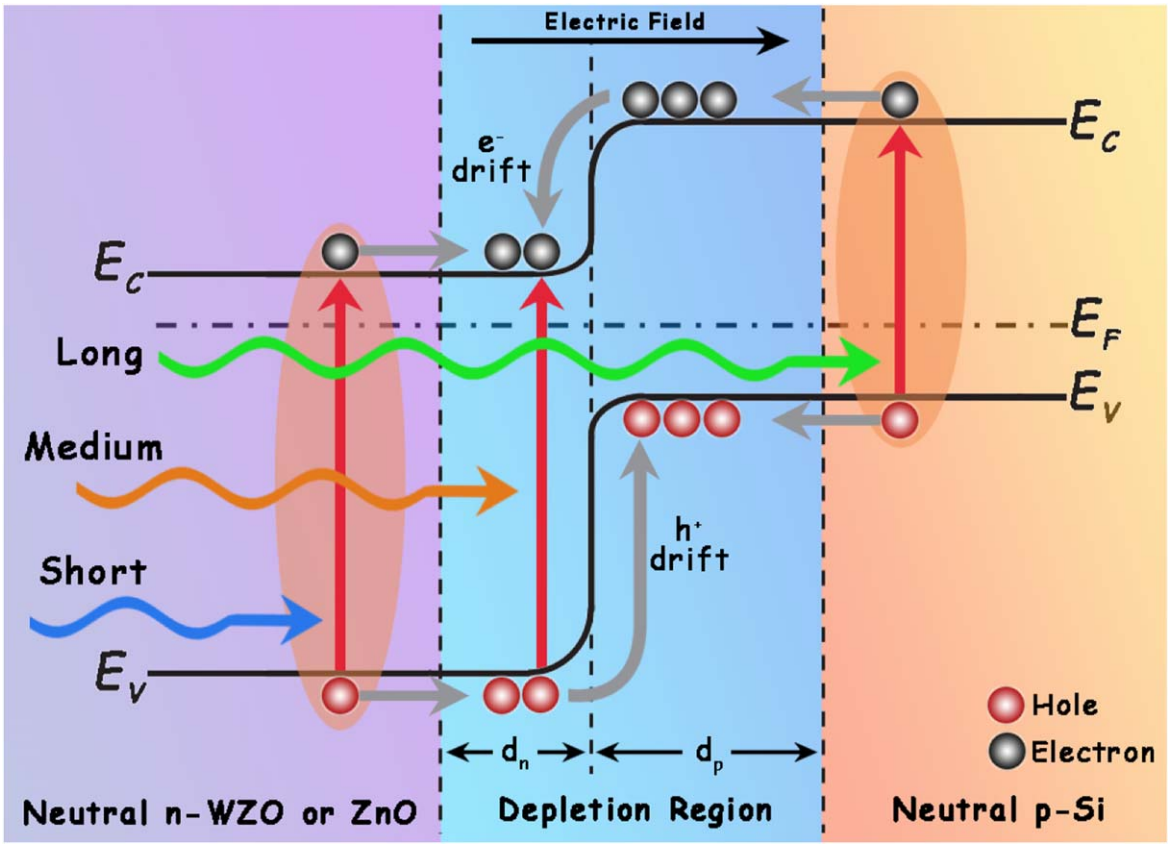


Figure 10. Energy band diagram of W-ZnO/*p*-Si under illumination condition at zero bias.

Table 5. A comparison of key parameters of *p*–*n* heterojunction-based photodetectors containing doped metal oxides.

Sample	τ_r(s)	*PR* (A/W)	*PS*	*D*∗ (Jones)	*EQE* (%)	References
ZnO:Y/Si	30	0.18	1356	3.93×10^{11}	—	[54]
CuO:Sr/Si	—	2.85	—	2.80×10^{12}	279	[55]
Ga_2O_3:Sb/Si	0.07	0.21	1600	—	103	[56]
TiO_2:Nb/Si	0.73	1.44	—	9.02×10^{12}	464	[57]
TiO_2:Er/Si	0.10	1.34	<15	5.76×10^{9}	—	[58]
CdO:Zn:Y/Si	0.80	1.45		6.00×10^{9}	339	[59]
Ga_2O_3:Ti/Si	0.073	0.38	—	2.30×10^{10}	130	[60]
ZnO:In/Si	—	1.07	—	8.40×10^{10}	<300	[61]
ZnO:W/Si	0.025	3.84	34.01	3.30×10^{12}	1305	This work

applied bias voltage, the dielectric constant values of the *n*-ZnO and *p*-Si, respectively. Additionally, the creation of a heterojunction between *n*-ZnO and *p*-Si is implied by the linear behavior of the *C*–*V* characteristics. The obtained values of V_{bi} and N_d are listed in table 4. Both parameters increase with increasing W-dopant ratio. Knowing V_{bi} allows us to determine the depletion layer width in the *n*-type region (d_n) and *p*-type region (d_p) [53],

$$d_n = \sqrt{\frac{2\varepsilon_1\varepsilon_2 V_{bi} N_a}{qN_d(N_d\varepsilon_1 + N_a\varepsilon_2)}} \tag{9}$$

$$d_p = \sqrt{\frac{2\varepsilon_1\varepsilon_2 V_{bi} N_d}{qN_a(N_d\varepsilon_1 + N_a\varepsilon_2)}} \tag{10}$$

Based on the data, the calculated depletion layer ($W=d_n+d_p$) varies between 482 and 513 nm and always $d_n < d_p$, indicating that the depletion layer is mainly located on the *p*-Si side. Expanding the depletion zone into Si results in the effective collection of carriers created by light illumination in the Si absorption region. This may enhance the transport and carrier separation properties in the depletion zone. One might expect that the device with 4 at% of W dopant would exhibit the best performance. However, the possibility of recombination of electron–hole pairs will be promoted due to the significantly increased concentration of charge carriers ($N_d = 1.03\times10^{17}\text{cm}^{-3}$) with 4 at% of W dopant, which hinders the development of performance of the device. In the fabricated devices, ultimately, in the device with 2 at% of W

dopant, the separation of the photogenerated carriers by incident light remains more effective.

Figure 10 presents the energy band diagram for the fabricated devices under light illumination. Due to the difference in Fermi levels, once Si and ZnO come in contact, electrons will diffuse from ZnO to Si (holes will diffuse in the other direction). The energy band will bend when both Fermi levels are in alignment, creating the depletion zone and built-in potential at the interface. Between Si and ZnO, a type II contact eventually develops. The potential barriers and depletion zone may be weakened when a forward bias is given to the *p–n* junction. Once UV light impinges onto the device, the light passes into the interface of the ZnO/Si *p–n* heterojunction and generates electron–hole pairs, causing the photodetector to have a significant photocurrent.

To vividly compare the photodetector performance of current work with those reported for *p–n* heterojunction-based photodetectors containing doped metal oxides (MO), finally, the key parameters of the MO:X (X: dopant)/Si *p–n* junction devices are summarized in table 5. In comparison, the overall performance of the W-doped ZnO/Si heterojunction photodetector is generally better than that of the previously reported devices. The present photodetector specifically outperforms them with a higher *PR*, a larger *EQE* and a shorter τ_r, implying that the W-doped ZnO/Si structured device is a promising candidate for high-performance UV-detecting applications.

4. Conclusion

In the present study, we investigated the optical, structural and electrical characteristics of W-doped ZnO/Si based photodetectors by focusing on the effect of varying the W content. W-doped ZnO thin films with different W content varying from 0 at% to 4 at% were deposited on Si substrates via sol–gel spin coating method. The current–voltage characteristics of the fabricated W-doped ZnO/Si *p–n* heterojunction-based photodetectors were measured in the dark and under UV illumination. It is observed that all the fabricated devices show diode-like rectifying behavior and UV detection property. Among them, sample with atomic ratio of W/Zn = 2% is the best performing UV photodetector, exhibiting a high PR of 3.84 A W^{-1} and a large *EQE* of 1305%. Moreover, it is noteworthy to say that the UV detection performance of the *p–n* heterojunction-based photodetectors strongly dependent on the properties of metal oxide layer and the nature of depletion zone. Ultimately, our results suggest that 2 at% of W dopant is the more suitable amount of doping for high performance photodetector of ZnO:W/Si heterojunction thanks to the suppressed recombination ratio and enhanced carrier separation properties in the depletion zone. In conclusion, our findings show that 2 at% of the W dopant is the optimum amount of doping for the high-performance photodetector of the ZnO:W/Si heterojunction, owing to the suppressed recombination rate together with the improved carrier separation and transport properties in the depletion region.

Acknowledgments

This work is based on R J's PhD thesis.

Data availability statement

The data cannot be made publicly available upon publication because no suitable repository exists for hosting data in this field of study. The data that support the findings of this study are available upon reasonable request from the authors.

ORCID iDs

K Ozel https://orcid.org/0000-0002-0250-3731

References

[1] Qin Y, Li L H, Yu Z, Wu F, Dong D, Guo W and Long S 2021 Ultra-high performance amorphous Ga_2O_3 photodetector arrays for solar-blind imaging *Adv. Sci.* **8** 2101106
[2] Zhao Z, Liu J, Liu Y and Zhu N 2017 High-speed photodetectors in optical communication system *J. Semiconduct.* **38** 121001
[3] Ozel K and Yildiz A 2020 SnO_2/ZnO/p-Si and SnO_2/TiO_2/p-Si heterojunction UV photodiodes prepared using a hydrothermal method *Sensors Actuators* A **315** 112351
[4] Ozel K, Atilgan A, Koksal N E and Yildiz A 2020 A route towards enhanced UV photo-response characteristics of SnO_2/p-Si based heterostructures by hydrothermally grown nanorods *J. Alloys Compd.* **849** 156628
[5] Al-Hardan N H, Jalar A, Hamid M A, Keng L K, Ahmed N M and Shamsudin R 2014 A wide-band UV photodiode based on n-ZnO/p-Si heterojunctions *Sensors Actuators* A **207** 61–6
[6] Leung Y H, He Z B, Luo L B, Tsang C H A, Wong N B, Zhang W J and Lee S T 2010 ZnO nanowires array pn homojunction and its application as a visible-blind ultraviolet photodetector *Appl. Phys. Lett.* **96** 053102
[7] Alenezi M R, Alshammari A S, Alzanki T H, Jarowski P, Henley S J and Silva S R P 2014 ZnO nanodisk based UV detectors with printed electrodes *Langmuir* **30** 3913–21
[8] Ozel K and Yildiz A 2022 Estimation of maximum photoresponsivity of n-SnO2/p-Si heterojunction-based UV photodetectors *Phys. Status Solidi (RRL)–Rapid Res. Lett.* **16** 2100490
[9] Li H, Huang J, Zheng Q and Zheng Y 2020 Flexible ultraviolet photodetector based ZnO film sputtered on paper *Vacuum* **172** 109089
[10] Kumari P, Srivastava A, Sharma R K, Sharma D and Srivastava S K 2022 Zinc oxide: a fascinating material for photovoltaic applications *Nanomaterials for Innovative Energy Systems and Devices* (Springer Nature) pp 173–241
[11] Huang K, Tang Z, Zhang L, Yu J, Lv J, Liu X and Liu F 2012 Preparation and characterization of Mg-doped ZnO thin films by sol–gel method *Appl. Surf. Sci.* **258** 3710–3
[12] Chanda A, Gupta S, Vasundhara M, Joshi S R, Mutta G R and Singh J 2017 Study of structural, optical and magnetic properties of cobalt doped ZnO nanorods *RSC Adv.* **7** 50527–36
[13] Amiruddin R and Santhosh Kumar M C 2017 High-speed photoresponse properties of ultraviolet (UV) photodiodes

using vertically aligned Al: ZnO nanowires *Phys. Status Solidi* (a) **214** 1600658
[14] Wang T, Chen J, Chen J, Yao X, Chen G, Jiao Z and Li Q 2023 UV-light enhanced gas sensor based on Ga doped ZnO for ultra-high sensitive and selective n-butanol detection *Appl. Surf. Sci.* **641** 158551
[15] Serin T, Yildiz A, Uzun Ş, Çam E and Serin N 2011 Electrical conduction properties of In-doped ZnO thin films *Phys. Scr.* **84** 065703
[16] Atilgan A, Kurtulus A Y, Oktem M F and Yildiz A 2021 W-doped ZnO transparent conducting nanostructures synthesized by hydrothermal method *J. Mater. Sci., Mater. Electron.* **32** 19126–35
[17] Lin L, Cheng C P and Teng T P 2016 Electrodeposition-based fabrication and characteristics of tungsten trioxide thin film *J. Nanomater.* **2016** 3623547
[18] Sajjad A K L, Shamaila S, Tian B, Chen F and Zhang J 2009 One step activation of WO_x/TiO_2 nanocomposites with enhanced photocatalytic activity *Appl. Catal.* B **91** 397–405
[19] Chen H K, Chen W F, Koshy P, Adabifiroozjaei E, Liu R, Sheppard L R and Sorrell C C 2016 Effect of tungsten-doping on the properties and photocatalytic performance of titania thin films on glass substrates *J. Taiwan Inst. Chem. Eng.* **67** 202–10
[20] Senthilkumar P, Raja S, Babu R R and Vasuki G 2022 Enhanced electrical and optoelectronic properties of W doped SnO_2 thin films *Opt. Mater.* **126** 112234
[21] Kamaruddin S A, Chan K Y, Yow H K, Zainizan Sahdan M, Saim H and Knipp D 2011 Zinc oxide films prepared by sol–gel spin coating technique *Appl. Phys.* A **104** 263–8
[22] Li Y, Xu L, Li X, Shen X and Wang A 2010 Effect of aging time of ZnO sol on the structural and optical properties of ZnO thin films prepared by sol–gel method *Appl. Surf. Sci.* **256** 4543–7
[23] Varol S F, Babür G, Çankaya G and Kölemen U 2014 Synthesis of sol–gel derived nano-crystalline ZnO thin films as TCO window layer: effect of sol aging and boron *RSC Adv.* **4** 56645–53
[24] Speaks D T 2020 Effect of concentration, aging, and annealing on sol gel ZnO and Al-doped ZnO thin films *Int. J. Mech. Mater. Eng.* **15** 1–14
[25] Serin T, Yildiz A, Şahin Ş H and Serin N 2011 Extraction of important electrical parameters of CuO *Physica*B **406** 575–8
[26] Ali D, Butt M Z, Arif B, Al-Ghamdi A A and Yakuphanoglu F 2017 The role of Al, Ba, and Cd dopant elements in tailoring the properties of *c*-axis oriented ZnO thin films *Physica* B **506** 83–93
[27] Ali D, Butt M Z, Coughlan C, Caffrey D, Shvets I V and Fleischer K 2018 Nitrogen grain-boundary passivation of In-doped ZnO transparent conducting oxide *Phys. Rev. Mater.* **2** 043402
[28] Ali D, Butt M Z, Muneer I, Farrukh M A, Aftab M, Saleem M and Khan A U 2019 Synthesis and characterization of sol-gel derived La and Sm doped ZnO thin films: a solar light photo catalyst for methylene blue *Thin Solid Films* **679** 86–98
[29] Manjula N, Pugalenthi M, Nagarethinam V S, Usharani K and Balu A R 2015 Effect of doping concentration on the structural, morphological, optical and electrical properties of Mn-doped CdO thin films *Mater. Sci. Poland* **33** 774–81
[30] Serin N, Yildiz A, Alsaç A A and Serin T 2011 Estimation of compensation ratio by identifying the presence of different hopping conduction mechanisms in SnO_2 thin films *Thin Solid Films* **519** 2302–7
[31] Ozel K 2023 Strain-induced photoresponsivity in gallium-doped ZnO thin film based UV photodetectors *Sensors Actuators*A **366** 114953
[32] Gordon R G 2000 Criteria for choosing transparent conductors *MRS Bull.* **25** 52–7
[33] Kumar P R, Kartha C S, Vijayakumar K P, Abe T, Kashiwaba Y, Singh F and Avasthi D K 2004 On the properties of indium doped ZnO thin films *Semicond. Sci. Technol.* **20** 120
[34] Li X Y, Li H J, Wang Z J, Xia H, Xiong Z Y, Wang J X and Yang B C 2009 Effect of substrate temperature on the structural and optical properties of ZnO and Al-doped ZnO thin films prepared by dc magnetron sputtering *Opt. Commun.* **282** 247–52
[35] Ammaih Y, Lfakir A, Hartiti B, Ridah A, Thevenin P and Siadat M 2014 Structural, optical and electrical properties of ZnO: Al thin films for optoelectronic applications *Opt. Quantum Electron.* **46** 229–34
[36] Koksal N E, Sbeta M and Yildiz A 2019 GZO/Si photodiodes exhibiting high photocurrent-to-dark-current ratio *IEEE Trans. Electron Devices* **66** 2238–42
[37] Ozel K and Yildiz A 2021 The potential barrier-dependent carrier transport mechanism in n-SnO_2/p-Si heterojunctions *Sensors Actuators* A **332** 113141
[38] Al-Hardan N H, Mohd Rashid M M, Abdul Aziz A and Ahmed N M 2019 Low power consumption UV sensor based on n-ZnO/p-Si junctions *J. Mater. Sci., Mater. Electron.* **30** 19639–46
[39] H. J, Lu Y, Li B, Tang K, Ma Y, Cao M, Wang L and Wang L 2018 A boron and gallium co-doped ZnO intermediate layer for ZnO/Si heterojunction diodes *Appl. Surf. Sci.* **428** 61–5
[40] Ozel K and Yildiz A 2021 A self-powered ultraviolet photodetector with ultrahigh photoresponsivity (208 mA W − 1) based on SnO_2 nanostructures/Si heterojunctions *Phys. Status Solidi (RRL)–Rapid Res. Lett.* **15** 2100085
[41] Chauhan K R and Patel D B 2019 Functional nanocrystalline TiO_2 thin films for UV enhanced highly responsive silicon photodetectors *J. Alloys Compd.* **792** 968–75
[42] Ozel K and Yildiz A 2021 High-detectivity ultraviolet-B photodetector based on SnO_2 thin film/Si heterojunction *Semicond. Sci. Technol.* **36** 095001
[43] Ghosh S, Varghese A, Thakar K, Dhara S and Lodha S 2021 Enhanced responsivity and detectivity of fast WSe_2 phototransistor using electrostatically tunable in-plane lateral pn homojunction *Nat. Commun.* **12** 3336
[44] Abbasi F, Zahedi F and hasan Yousefi M 2021 Fabricating and investigating high photoresponse UV photodetector based on Ni-doped ZnO nanostructures *Opt. Commun.* **482** 126565
[45] Shkir M 2022 Enhancement in optical and electrical properties of ZnO thin films via Co doping for photodetector applications *Mater. Sci. Eng.* B **284** 115861
[46] Kumar M, Bhatt V, Abhyankar R A, Kim J, Kumar A and Yun J H 2018 Modulation of structural properties of Sn doped ZnO for UV photoconductors *Sensors Actuators* A **270** 118–26
[47] Kumar K D A, Mele P, Murahari P, Abdeltawab A A, Mohammady S Z, Ubaidullah M and AlFaify S 2022 Enhancement of performance of Ga incorporated ZnO UV photodetectors prepared by simplified two step chemical solution process *Sensors Actuators* A **333** 113217
[48] Raj I L P, Valanarasu S, Hariprasad K, Ponraj J S, Chidhambaram N, Ganesh V and Khairy Y 2020 Enhancement of optoelectronic parameters of Nd-doped ZnO nanowires for photodetector applications *Opt. Mater.* **109** 110396
[49] Kumar C, Kushwaha B K, Kumar A, Jarwal D K, Upadhyay R K, Singh A P and Jit S 2020 Fibrous Al-doped ZnO thin film ultraviolet photodetectors with improved responsivity and speed *IEEE Photon. Technol. Lett.* **32** 337–40
[50] Abbasi F, Zahedi F and Yousefi M H 2021 Performance improvement of UV photodetectors using Cd-doped ZnO nanostructures *J. Mater. Sci., Mater. Electron.* **32** 19614–25

[51] Chu Y L, Young S J, Ji L W, Tang I T and Chu T T 2020 Fabrication of ultraviolet photodetectors based on Fe-doped ZnO nanorod structures *Sensors* **20** 3861
[52] Ozel K and Yildiz A 2021 Comprehensive understanding of the role of emitter layer thickness for metal–oxide–semiconductors based solar cells *IEEE J. Photovolt.* **12** 251–8
[53] Su L, Zuo Y and Xie J 2021 Scalable manufacture of vertical p-GaN/n-SnO2 heterostructure for self-powered ultraviolet photodetector, solar cell and dual-color light emitting diode *InfoMat* **3** 598–610
[54] Saha R, Dalapati G K, Chakrabarti S, Karmakar A and Chattopadhyay S 2022 Yttrium (Y) doped ZnO nanowire/p-Si heterojunction devices for efficient self-powered UV-sensing applications *Vacuum* **202** 111214
[55] Hassan M A, Mohsin M H and Ismail R A 2023 Preparation of high-responsivity strontium–doped CuO/Si heterojunction photodetector by spray pyrolysis. *J. Mater. Sci., Mater. Electron.* **34** 912
[56] Feng Q J, Yu C, Yi Z Q, Sui X, Wang Y M, Wang S and Laing H W 2023 Study of self-powered UV detector based on Sb-doped β-Ga_2O_3 thin film/P–Si heterojunction *Opt. Mater.* **145** 114431
[57] Yadav P K, Ajitha B, Ahmed C M A, Reddy Y A K and Reddy V R M 2022 Superior UV photodetector performance of TiO_2 films using Nb doping *J. Phys. Chem. Solids* **160** 110350
[58] Mondal S, Ghosh C, Dwivedi S D, Ghosh A, Sushama S, Chakrabarti S and Mondal A 2021 An experimental and theoretical understanding of a UV photodetector based on Ag nanoparticles decorated Er-doped TiO_2 thin film *Ceram. Int.* **47** 14879–91
[59] Babu R S, Murthy Y N, Raj I L P, Revathy M S, Chidhambaram N, Ganesh V and Yahia I S 2021 Improved optoelectronic properties of Yttrium co-doped CdO:Zn thin films fabricated by nebulizer spray pyrolysis method for TCO applications *Phys. Scr.* **96** 125860
[60] Harmanci U, Gulluoglu M T, Aslan F, Atilgan A and Yildiz A 2022 Solar-blind ultraviolet photodetector based on Ti-doped Ga_2O_3/Si *p–n* heterojunction *J. Mater. Sci., Mater. Electron.* **33** 20223–8
[61] Adaikalam K, Valanarasu S, Ali A M, Sayed M A, Yang W and Kim H S 2022 Photosensing effect of indium-doped ZnO thin films and its heterostructure with silicon *J. Asian Ceram. Soc.* **10** 108–19